JACS
JOURNAL OF THE AMERICAN CHEMICAL SOCIETY

ARTICLE

pubs.acs.org/JACS

Fabrication of All-Inorganic Nanocrystal Solids through Matrix Encapsulation of Nanocrystal Arrays

Erich Kinder,[‡,§] Pavel Moroz,[†,‡,§] Geoffrey Diederich,[‡] Alexa Johnson,[†,‡] Maria Kirsanova,[†,‡] Alexander Nemchinov,[†,‡] Timothy O'Connor,[‡] Dan Roth,[‡] and Mikhail Zamkov*[,†,‡]

[†]The Center for Photochemical Sciences and [‡]Department of Physics, Bowling Green State University, Bowling Green, Ohio 43403, United States

Supporting Information

ABSTRACT:

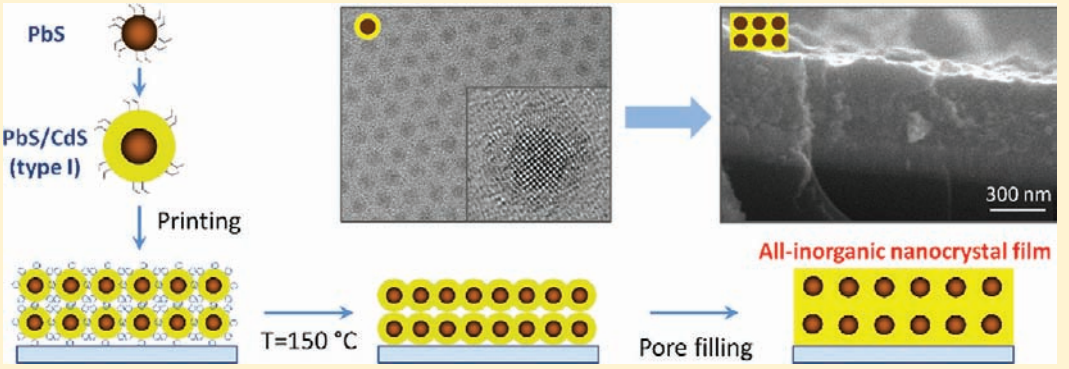

A general strategy for low-temperature processing of colloidal nanocrystals into all-inorganic films is reported. The present methodology goes beyond the traditional ligand-interlinking scheme and relies on encapsulation of morphologically defined nanocrystal arrays into a matrix of a wide-band gap semiconductor, which preserves optoelectronic properties of individual nanoparticles while rendering the nanocrystal film photoconductive. Fabricated solids exhibit excellent thermal stability, which is attributed to the heteroepitaxial structure of nanocrystal−matrix interfaces, and show compelling light-harvesting performance in prototype solar cells.

INTRODUCTION

The development of semiconductor thin films from nanocrystal "inks" is emerging as a powerful alternative to conventional methods of film deposition relying on high-vacuum and high-temperature processing of bulk semiconductors. In addition to the anticipated cost reduction, the integration of solution-processed nanocrystal (NC) films into device architectures is inspired by the possibility of tuning the energy of electrical charges in NCs via nanoparticle size. This opens up an additional degree of freedom for manipulating material's optoelectronic properties and controlling charge flow rates at heterostructured interfaces. Owing to these advantages, the deployment of semiconductor NC films in device technologies has been actively explored in the past decade through the demonstration of a wide range of NC-based applications, including lasers,[1−3] solar cells,[4−26] photocatalysts,[27−31] light-emitting diodes (LEDs),[32−39] biolabels,[40−42] thermoelectric elements,[43,44] field-effect transistors,[45−50] and magnetic[51,52] and memory elements.[53−57]

Over the years, several strategies for assembling NCs into functional films (also known as NC solids) have been explored. To improve electrical coupling between neighboring nanoparticles, individual NCs in these films are often interlinked with molecular bridges, utilizing either organic molecules, such as short-chain dithiols,[58−61] butylamine,[62] ethylenediamine,[63] 3-mercaptopropionic acid (MPA),[64] hydrazine,[49] pyridine,[65,66] or inorganic metal chalcogenide complexes, such as Zintl ions.[44,67] Besides enhancing an electrical conductivity of the film, these molecules perform a role of surface-passivating ligands, the presence of which is critical for preserving carrier localization in NCs and protecting their surfaces from oxidation. For instance, a compelling electrical performance has been reported for PbS and PbSe NC solids cross-linked with hydrazine, MPA, or 1,2-ethanedithiol (EDT)[68] molecules. For these films the mobility of charge carriers reached a compelling 0.1−0.7 $cm^2/(V\cdot s)$ level,[73] which merits the performance of thin-layer devices (l < 200 nm), such as solar cells, with reported power conversion efficiency (PCE) of up to 5.1%.[64,69] Meanwhile, the use of inorganic Zintl ion linkers,[67] or recently reported Al_2O_3 infilling of organically linked nanocrystals[70] have been demonstrated to improve the overall

Received: September 14, 2011
Published: November 14, 2011

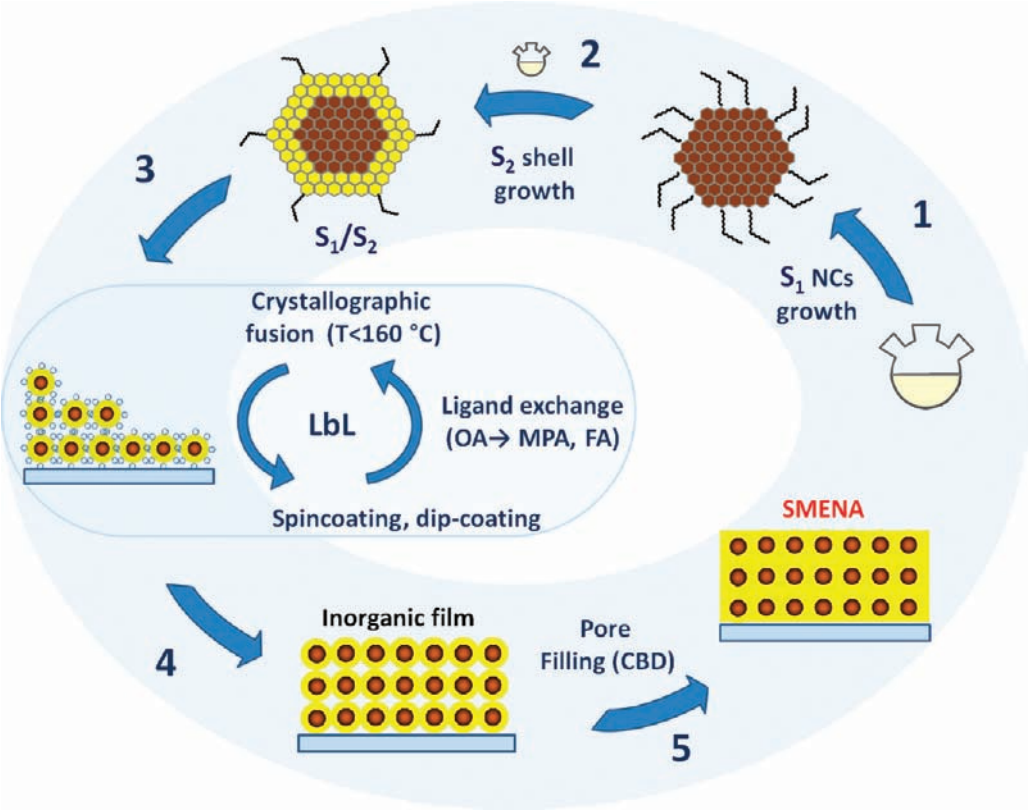

Figure 1. Flow chart showing the key steps involved in development of semiconductor matrix-encapsulated nanocrystal arrays (SMENA). These stages include colloidal synthesis of PbS NCs (step 1), growth of the CdS shell (step 2), and spin-coating or dip-coating of NC films, exchange of bulky ligands with thermally degradable molecules (MPA, FA), and crystallographic fusion of NCs, all three performed via layer-by-layer deposition (steps 3 and 4). In the last step, the pores of the PbS/CdS solid are filled with an additional CdS or ZnS material (step 5). In several cases, surfaces of the resulting matrix were further passivated with $ZnCl_2$ or Br (see Experimental Section).

stability of the film. Despite these advances, the development of functional NC solids still faces several important challenges that need to be properly addressed before electrical characteristics of these films can effectively compete with the rival technologies based on amorphous silicon[71] or organic polymer films.[72]

At present, the key factors limiting the competitiveness of NC devices are identified as the *poor stability* of NC films in heated or oxygenated environments, which dramatically impacts the cost–effect characteristics of these materials in heat-intensive applications (solar cells, photodetectors, and LEDs), and the relatively *low mobility of electrical charges* [$\sim$1 $cm^2/(V\cdot s)$],[73,74] which leads to substantial energy losses in thick-layer devices due to charge trapping and side reactions. Notably, both of these issues are related to the nature of the interlinking mechanism in NC films and not to the properties of isolated nanoparticles. Indeed, the ligands that connect neighboring NCs in the film are attached to NC surfaces through a donor–acceptor interaction and, therefore, can readily desorb when electrically or thermally stimulated. Detachment of even a small fraction of these ligands can lead to significant changes in the film performance due to the formation of trap states,[39,75] NC oxidation, and the subsequent deterioration of the semiconductor lattice. Furthermore, dissociation of ligands has been claimed to trigger the removal of surface cations from the NC,[76] which leaves behind anion-terminated surface associated with deep level surface traps.

Here we address the aforementioned limitations of ligand-bound NC solids through the development of an alternative film processing strategy that goes beyond the traditional cross-linking scheme and employs a thermally and chemically stable, all-inorganic medium to encase morphologically defined NC arrays. Here, this strategy is demonstrated by encapsulating PbS NC arrays into a matrix of a wide-band gap semiconductor (CdS, ZnS), which preserves some degree of quantum confinement in PbS nanoparticles yet enables both electrical conductivity of the film, tunable via inter-NC spacing, and excellent thermal/chemical stability of resulting solids, facilitated by the heteroepitaxial capping of PbS NCs with the matrix material (e.g., CdS).

The matrix encapsulation strategy relies on low-temperature (T < 160 °C) processing of semiconductor NCs, performed by spin-coating or dip-coating techniques. Specifically, to incorporate an array of S_1 semiconductor NCs (e.g., PbS NCs) into a matrix of a wide band gap semiconductor material (S_2), colloidal S_1 NCs are first overcoated with several monolayers (ML) of S_2, yielding type I core/shell hetero-NCs, S_1/S_2, (e.g., PbS/CdS or PbS/ZnS), as shown in Figure 1. Subsequently, S_1/S_2 nanoparticles are thermally fused into all-inorganic heteroepitaxial arrays, for which charge-confining S_1 cores (PbS NCs) are encased within the matrix of the cross-merged shell material, S_2 (Figure.1, step 3). To promote a crystallographic fusion of core/shell NCs into a porous solid, at temperatures that preserve S_1 domains but allow for the respective shells (S_2) to be brought together through quasi-epitaxial bonding, spin-coated films of S_1/S_2 core/shell NCs are capped with low-boiling-point ligands (T < 110 °C) and subjected to heating at 120–160 °C. Following the ligand

desorption, the surfaces of S_2 semiconductor in the NC solid are treated with an additional S_2 material, which is deposited into the pores of the S_1/S_2 film via chemical bath deposition (CBD) or successive ionic layer adsorption and reaction (SILAR)[77] methods (Figure 1, step 5).

Electrical coupling between adjacent NCs in the resulting semiconductor matrix encapsulated nanocrystal arrays (SMENA) is controlled either by tuning the inter-NC separation between PbS cores (via S_2 shell thickness), or by varying the band gap of the matrix material (CdS, ZnS). An empirical model has been developed to provide a qualitative estimate of PbS−PbS coupling energy as a function of inter-NC separation and the band gap of the matrix semiconductor. We demonstrate that, in the regime of close coupling between 1S(e) states of PbS NCs, the films are rendered photoconductive and can be utilized as an active medium in NC solar cells. Meanwhile, for weakly coupled SMENA solids (Mott insulators), 1S(e) carriers are primarily site-localized, which gives rise to observable fluorescence from PbS cores. This could have important implications for the development of infrared-emitting thin-film waveguides.

The architecture of SMENA solids offers several unique advantages that could be of a substantial benefit to the development of NC devices. First, crystallographic fusion of S_1 and S_2 semiconductors into a heterostructured solid can potentially enable the construction of heteroepitaxial monoliths exhibiting a low density of lattice defects, which effectively reduces the trap state formation and minimizes carrier scattering, an important milestone toward increasing the conductivity of NC films. Second, encapsulation of S_1 NCs within a matrix of a lattice-matched semiconductor (S_2), provides an elegant approach for capping NC surfaces with a layer of an inorganic material exhibiting a greater degree of tolerance to heat and oxidation than traditional molecular ligands. Indeed, in contrast to surface molecules, the S_2 matrix (e.g., CdS or ZnS) is not prone to degradation in the ambient environment and thus will not allow oxygen attacks on S_1 surfaces. The improved stability of matrix-encapsulated NC solids is particularly important for the development of solar-absorber materials in light of the expected thermal loads that photovoltaic panels have to withstand in field conditions. Third, the SMENA morphology allows for a *continuous* optimization of the internanocrystal coupling,[78] $\beta \sim \exp[-\alpha(\Delta x)]$, tunable via the thickness of the S_2 shell ($\Delta x/2$).

EXPERIMENTAL SECTION

Materials. 1-Octadecene (ODE, 90%; Aldrich), oleylamine (OLAM, 70%; Aldrich), oleic acid (OA, 90%; Aldrich), hexadecyltrimethylammonium bromide (CTAB, 99%; Sigma), titanium tetrachloride ($TiCl_4$, 99.9%; Aldrich), titanium(IV) isopropoxide (99.999%; Aldrich), lead(II) nitrate [$Pb(NO_3)_2$, 99.99%; Aldrich], lead(II) oxide powder (PbO, 99.999%; Aldrich), sodium sulfide nonanhydrate ($Na_2S\cdot 9H_2O$, 98%; Alfa Aesar), sulfur (S, 99.999%; Acros), titanium dioxide (DSL 90T, DyeSol), selenium powder (Se, 99.5%; Acros), tellurium powder (Te, 99.8%; Aldrich), ethanol (anhydrous, 95%; Aldrich), methanol (anhydrous, 99.8%; Aldrich), toluene (anhydrous, 99.8%; Aldrich), 2-propanol (anhydrous, 99.8%; Acros), octane (anhydrous, 99%; Aldrich), 3-mercaptopropionic acid (3-MPA, 99%; Alfa Aesar), bis(trimethylsilyl) sulfide (TMS_2, synthetic grade; Aldrich), zinc chloride ($ZnCl_2$, 99.995%; Aldrich), tri-*n*-octylphosphine (97%, Strem), and Triton X-100 (Alfa Aesar) were used as received without any further purification. Regular acetone was distilled before use, and all reactions were performed under argon atmosphere by the standard Schlenk technique. Fluorine-doped tin oxide (FTO) glass (TEC 15, 12−14 Ω/sq) was obtained from Pilkington Glass.

Methods. *Synthesis of PbS NCs.* PbS NCs were fabricated according to a procedure adapted from ref 79. In a typical synthesis, a mixture of 0.49 g of PbO in 18 mL of ODE and 1−16 mL of OA (increasing the amount of OA results in larger NCs) was degassed in a three-neck flask at 120 °C for 2 h, switched to argon, and heated to 135 °C. In another flask, 10 mL of ODE was degassed for 2 h at 120 °C and allowed to cool down to room temperature, then 0.21 mL of TMS_2 was added carefully into the flask and the resulting TMS_2/ODE mixture was injected into the Pb precursor solution at 135 °C, while stirring. The reaction was stopped after 0−5 min (longer reaction time leads to larger NCs) by removing the flask from the heating mantle and placing it into an ice water bath. The nanocrystals were isolated from the mixture by precipitating with distilled acetone, centrifuging, and redispersing in toluene. The cleaning procedure was repeated 2−3 times, after which nanocrystals were redispersed in a minimal amount of octane or toluene (4−5 mL).

For example, to fabricate PbS NCs with an exciton absorption feature centered at 1140 nm, 14 mL of OA was used and the growth time was limited to 3 min. For NCs with a 1S peak at 1750 nm, 14 mL of OA was used with a growth time of 6 min. For NCs with a 1S peak at 930 nm, 1.5 mL of OA was used with a reaction time of 1 min.

Synthesis of PbS/CdS Core/Shell NCs through Cation Exchange. Growth of the CdS shell on PbS NCs was performed by a cation-exchange methodology.[80] To this end, 1 g of CdO was combined with 6 mL of OA and 15 mL of ODE in a one-neck 50 mL flask. This mixture was heated at 280 °C under argon until the solution turned almost clear, upon which the temperature was lowered down to 100 °C. Separately, in a three-neck flask, 20−40 mg of PbS NCs dissolved in toluene were heated under argon to 110 °C for less than 5 min to evaporate most of the excess solvent, and the contents of the Cd precursor flask were added. The mixture was then heated to between 120 and 160 °C depending on the desired shell thickness. The reaction was stopped when the final temperature was reached by placing the flask in an ice bath. PbS/CdS NCs were isolated by adding ethanol and centrifuging at 5000 rpm. The liquid layer was discarded, and the precipitate was redissolved in toluene. This procedure was repeated two more times. NCs were finally redispersed in 2−3 mL of anhydrous octane.

The following example illustrates how the reaction temperature affects the growth of the CdS shell, in which evolution is measured as a blue shift of the PbS exciton absorbance. To achieve a blue shift of $\Delta\lambda$ = 140 nm (approximately 0.55 nm of the CdS shell), the mixture was allowed to reach 110 °C in 5 min. For a blue shift of $\Delta\lambda$ = 220 nm, the temperature was allowed to increase to 130 °C. For a shift of $\Delta\lambda$ = 45 nm, the reaction was immediately quenched in an ice water bath after injection of the Cd precursor into the PbS NC solution.

Preparation of TiO_2 on FTO/Glass Substrates. FTO-coated glass was cut into 2.5 cm × 2.5 cm squares, then washed by hand with detergent (Alconox), and rinsed clean in deionized water. It was then sonicated in methanol, acetone, and 2-propanol for 5 min in each solvent. Once dry, the substrate was placed in a bath of 75 mM $TiCl_4$ solution in deionized water and was heated (in air) for 30 min at 70 °C. The substrate was then rinsed with deionized water, dried under argon, heated to 450 °C for 1 h, and then allowed to cool to room temperature. Meanwhile, the TiO_2 DyeSol paste was dissolved in terpinol in a 1:3 ratio by weight. Three drops of the TiO_2 solution was placed in the center of a dry $TiCl_4$-treated FTO/glass slide and spun for 6 s at 700 rpm and for 1 min at 2000 rpm. The substrate was then annealed outside the glovebox (ambient oxygen environment) at 450−500 °C to remove organic matter.

Fabrication of PbS/CdS NCs from Solution. To fabricate an all-inorganic film of PbS/CdS NCs, layer-by-layer methodology was employed. All steps were performed inside the glovebox. Typically, 4−5 drops of PbS/CdS NCs in octane (concentration 10 mg/mL) were

placed onto a still TiO_2/FTO glass slide and allowed to spread until the substrate was covered. The NC solution was left to soak until the center dried and then spun at 2500 rpm for 30 s. Next, 10 drops of a 1:3 MPA/methanol solution was placed on the film, fully covering the surface, which was then spun at 2500 rpm for 15 s. The film was washed with 10 drops of methanol and subsequently spun at 2500 rpm until dry, then washed once again with 10 drops of octane in the same manner. The film was annealed at 150−160 °C for 15 min after every three layers. Overall, 8−10 layers were needed to form a 300-nm SMENA film. The OA → formic acid (FA) ligand exchange processed was performed by a dip-coating approach. Typically, upon spin-coating of 4 drops of PbS/CdS NCs onto an FTO/glass substrate, the sample was placed into a 10 mM solution of FA in acetonitrile for 1 min and then rinsed with dry acetonitrile for 1 min.

Infilling of SMENA Pores with CdS. To deposit CdS into the pores of an annealed, all-inorganic PbS/CdS film, a cadmium bath was prepared by dissolving 0.43 g of cadmium acetate in 80 mL of methanol. The sulfur bath was made by combining 0.38 g of $Na_2S \cdot 9H_2O$ with 80 mL of methanol. The sample was placed in the cadmium bath for 1 min, rinsed with methanol for 1 min, placed in the sulfur bath for 1 min, and finally washed in methanol again. This process was repeated 2−16 times, depending on the desired number of CdS monolayers. The film was then annealed at 150 °C for 15 min. For infilling with ZnS, 0.34 g of zinc acetate in 80 mL of methanol was used in place of Cd.

Passivation of SMENA Surfaces. To passivate CdS or ZnS surfaces of SMENA films, two different strategies were used. As one option, $ZnCl_2$ treatment of fabricated films was employed. To initiate this procedure, a combination of 0.1 M $ZnCl_2$ and 0.1 M HCl in water was prepared. The sample was placed in the HCl/$ZnCl_2$ solution for 1 min and then rinsed with deionized water. The cells were subsequently heated under argon to 150 °C for 15 min. The second surface passivation strategy was based on recently reported CTAB treatment,[69] which leaves Cd^{2+} cations terminated with Br. Typically, following the SILAR infilling step, 0.25 mL of CTAB (concentration 10 mg/mL) was placed on the film and allowed to sit for 1 min, rinsed with 10 drops of methanol, and spun until dry. This was repeated one more time.

Deposition of Au−Pd Counterelectrodes. To complete the cell assembly, 20−60 nm of gold−palladium (Au−Pd, 40/60) counterelectrodes were coated on top of the film via Polaron E500 sputter, which was equipped with a ≈2-mm diameter shadow mask generating 16 pixels in each device. The area of each pixel was estimated to be 0.03 cm^2.

Preparation of Best-Performing Solar Cell (η = 2.3%). Construction of the cell was initiated with the FTO cleaning procedure and a subsequent deposition of a TiO_2 layer with $TiCl_4$ bath and TiO_2 DyeSol paste treatment steps, as described above. A sample of PbS/CdS core/shell nanocrystals (PbS/CdS nanoparticle diameter =3.60 nm, CdS shell thickness ≈ 0.25 nm, 1S absorption feature of the core at λ = 1020 nm) was prepared in octane in the concentration of ≈10 mg/mL. To deposit each layer, 5 drops of NCs in octane was placed on the slide and allowed to spread until it covered the substrate. The NC solution was left until the center dried and then spun at 2500 rpm for 15 s. Next, 10 drops a 1:3 solution of MPA in methanol was placed on the film so that the MPA covers the film, which was then spun at 2500 rpm for 15 s. The film was washed with 10 drops of methanol, spun at 2500 rpm until dry, and washed once again with 10 drops of octane in the same manner. Every third layer, the film was heated to 150 °C for 15 min. When nine cycles had been completed, the film had four cycles of pore filling with CdS, per the above instructions. After SILAR, 0.25 mL of CTAB (concentration 10 mg/mL) was placed on the film and allowed to sit for 1 min, spun dry, then rinsed with 10 drops of methanol and spun until dry. The films had approximately 60 nm of Au−Pd sputter coated as a back contact. Prior to any measurements being done, a small portion of the film was removed via a cotton swab soaked in acetone, until the FTO surface was exposed enough to make contact.

Characterization. Absorbance spectra were recorded on Cary 50 scan and Shimadzu UV-3600 UV−vis-NIR spectrophotometers. High-resolution transmission electron microscopy (HR-TEM) measurements were carried out on JEOL 3011UHR and 2010 transmission electron microscopes, operated at 300 and 200 kV, respectively. To prepare a TEM sample, a small amount of NC film was scraped, dispersed in toluene by sonication, dropped onto a carbon-coated copper grid, and allowed to dry in air. X-ray powder diffraction (XRD) measurements were carried out on a Scintag XDS-2000 X-ray powder diffractometer. Energy-dispersive X-ray (EDX) emission spectra were measured on an EDAX X-ray detector located inside the Inspect scanning electron microscope (SEM). The electron beam was accelerated at 10 kV. Current−voltage characteristics were performed under AM 1.5 G (100 mW/cm^2) solar simulator on the $I-V$ data acquisition system from PV Measurements, Inc., while the incident photon to charge carrier efficiency (IPCE) was measured on a home-built system comprising a xenon lamp, a CM110 1/8 m monochromator, and a SR-830 lock-in amplifier.

RESULTS AND DISCUSSION

A detailed description of the main steps (see Figure 1) involved in the preparation of CdS- and ZnS-encapsulated PbS NC arrays (SMENA) is provided in the Experimental Section. Briefly, hot-injection colloidal syntheses were used to fabricate nearly monodisperse PbS NCs ($\triangle d$ < 6%; Figure SF1, Supporting Information) according to a methodology adapted from ref 79. The CdS shell was subsequently grown on PbS NCs through a $Pb^{2+} \rightarrow Cd^{2+}$ cation-exchange reaction,[82,83] which relies on the replacement of an outer layer in PbS NCs with CdS, such that the size of nanoparticles does not change during growth. This allows preserving a low dispersion of nanocrystals diameters during the PbS → PbS/CdS transformation (SD 6% → 7%; Figure SF2, Supporting Information, and Figure 4a), as was exemplified by the demonstrated ability of PbS/CdS NCs to form ordered patterns upon solvent evaporation (Figure 4a). The thickness of the CdS shell was controlled with submonolayer precision by tuning the temperature of the growth solution during the cation-exchange reaction (see details in Experimental Section). According to the high-resolution (HR) TEM analysis of several PbS/CdS core/shell structures (Figure 2b and Figure SF2c, Supporting Information), CdS shell grew uniformly on the surface of PbS NCs without noticeable lattice defects, which was attributed to relatively low lattice stress at the interface of PbS and CdS crystal phases (strain ≈ 1.7%). A good lattice match at the core/shell boundary has also enabled the growth of large CdS shells totaling 14−16 monolayers (ML). Notably, even for large-diameter core/shell NCs comprising 14 MLs of CdS, HR-TEM examination did not reveal any evidence of stacking faults in the shell phase (Figure 2c), further confirming the existence of low-strain matching between PbS and CdS lattices.

The character of charge confinement in PbS/CdS core/shell NCs was substantiated on the basis of steady-state spectroscopy of excitonic transitions in these nanoparticles. According to Figure 2d, the $Pb^{2+} \rightarrow Cd^{2+}$ cation exchange in PbS NCs results in blue-shifting of the absorption and emission features, which is attributed to the decreased length of the carrier confinement in PbS cores. The magnitude of this spectral shift is proportional to the reduction in the PbS diameter (see eq SE1 and Figure SF1 in Supporting Information) and was used here for estimating the thickness of the PbS layer that was converted into the CdS shell. In addition to blue-shifting of excitonic transitions, the transformation of PbS NCs into PbS/CdS core/shell structures was

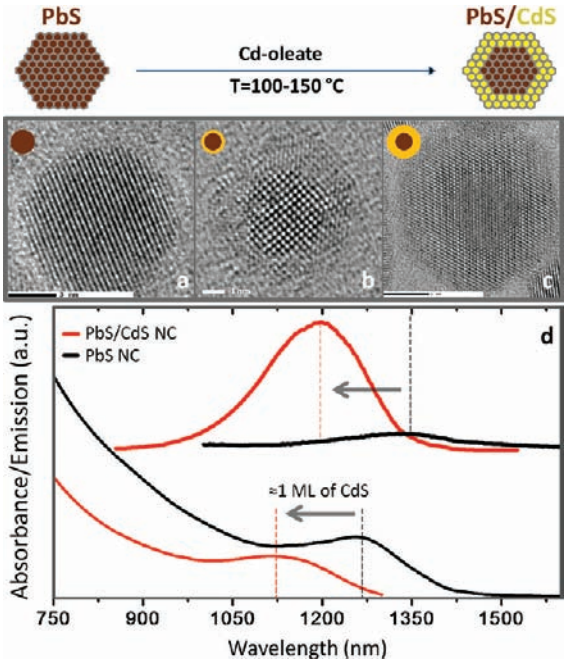

Figure 2. High-resolution TEM images showing formation of the CdS shell over PbS NCs during the cation-exchange reaction. (a) Oleic acid-capped PbS NC. (b) PbS NC coated with 4−5 monolayers of the CdS shell. (c) PbS NC coated with 12−14 ML shell of CdS. (d) Changes in the absorption and emission of PbS NCs resulting from deposition of approximately 1 ML of the CdS shell. Both features blue-shift by ≈150 nm, reflecting a decrease in the core diameter. The PbS fluorescence intensity is enhanced due to the formation of type I heterostructure.

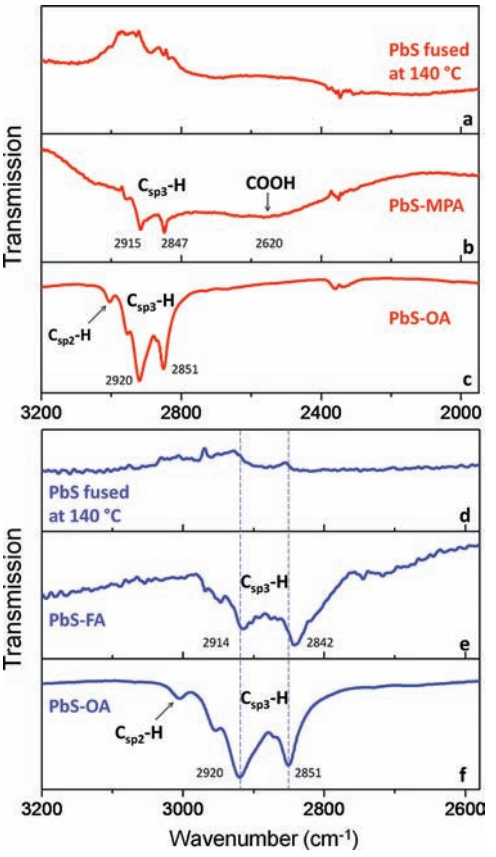

Figure 3. Fourier transform infrared spectroscopy (FTIR) analysis of the organic residue in NC solids. (a−c) Crystallographic fusion of MPA-capped PbS/CdS NCs. (c) A typical FTIR transmission spectrum of OA-capped PbS/CdS NCs in a film, showing characteristic C_{sp2}−H and C_{sp3}−H vibrational transitions of OA molecules. (b) The OA → MPA ligand exchange process is accompanied by the red shift of both C_{sp3}−H peaks and a simultaneous onset of the COOH feature at $k = 2620$ cm^{-1}. (a) FTIR spectrum of the NC film heated at 140 °C for 20 min, showing a significant reduction in the amplitude of MPA vibrational transitions. (d−f) Crystallographic fusion of FA-capped PbS/CdS NCs.

accompanied by a 5−10-fold increase in the emission intensity, which reflected a diminishing probability of core-localized charges to be trapped on NC surfaces. Such enhancement of the emission yield upon shell growth is consistent with the onset of type I carrier localization in PbS/CdS core/shell heterostructures, for which both electrons and holes reside primarily in the core domain of the composite NC. We note that core localization of photoinduced charges is important for the development of SMENA solids, as it allows preserving the quantum confinement of matrix-incorporated NCs and enables the tunability of excited-state energies via nanoparticle size.

To facilitate a low-temperature fusion of core/shell NCs into an all-inorganic film, the original, oleic acid (OA) ligands on NC surfaces were exchanged with thermally degradable molecules such as 3-mercaptopropionic acid (MPA, $T = 111$ °C) or formic acid (FA, $T = 101$ °C). Based on the fact that NCs form better "inks" when dressed with bulky OA ligands, the ligand exchange process was performed *after* the film deposition, which was achieved by exposing spin-coated solids of OA-capped NCs to a solution of a new ligand. Layer-by-layer (LbL) cycling[84] was employed to facilitate complete replacement of OA with MPA (FA) and to prevent cracking of the film due to the volume reduction. Typically, a 30-nm-thick layer of NCs was deposited in each LbL cycle, followed by treatment with a solution of an incoming ligand (MPA, FA) and subsequent heating of the film to approximately 140−160 °C. Special settings of the spin-coating process comprising both soaking and spinning stages were necessary for achieving good-quality films. Please see Experimental Section for more details. According to Fourier transform infrared (FTIR) measurements of NC films after the ligand exchange step, most of the original OA ligands were successfully replaced with MPA or FA molecules, as was attested by a 6−7 cm^{-1} red shift of C_{sp3}−H lines.[85] The subsequent thermal evaporation of MPA (FA) ligands resulted in quenching of the respective vibrational transitions (Figure 3c), confirming the removal of the organic phase from NC films. Desorption of organic ligands in films annealed at 140−160 °C was consistent with the observation of crystallographic fusion across adjacent NCs in electron microscope images (Figure 4h).

The effect of ligand desorption on the morphology of NC films was investigated by transmission electron microscopy (TEM). To perform a TEM analysis, fragments of annealed SMENA films were scratched from the FTO substrate with a needle tip, redissolved in toluene by sonicating for 15 min, and deposited onto a carbon grid from the solution. According to TEM images (Figure 4d,g), heating of MPA-capped NCs to as low as 100 °C promotes initial clustering, while annealing at 150 °C for 20 min results in the crystallographic fusion of neighboring NC shells, manifested by the formation of continuous fringe pattern across adjacent NCs (Figure 4h,f). For these films the excitonic features of encapsulated PbS NCs were clearly

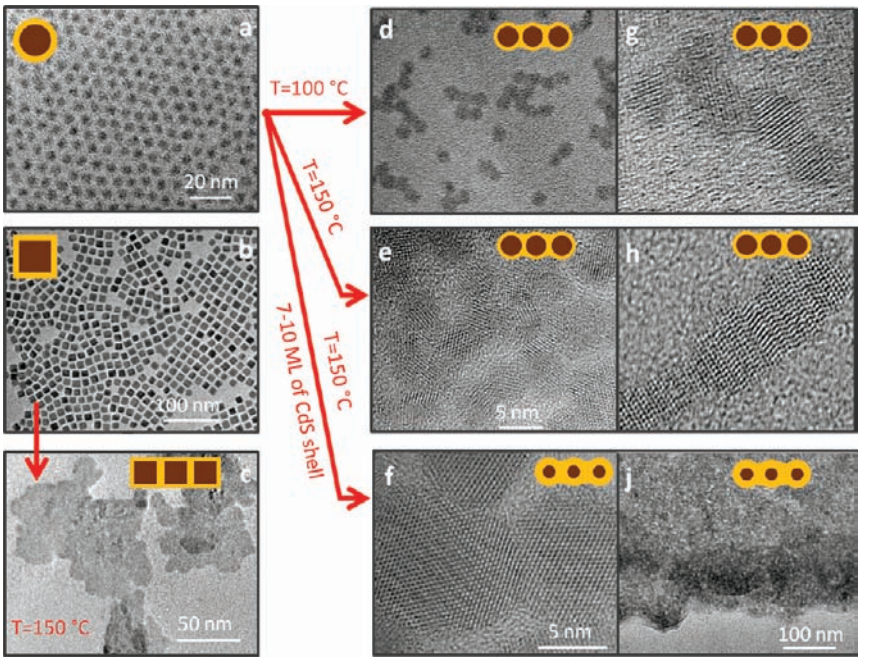

Figure 4. TEM images of PbS/CdS NCs and fragments of the SMENA. (a, b) PbS NCs capped with a thin shell of CdS (~1−2 ML). (c) A fragment of the SMENA solid fabricated via crystallographic fusion of cubic-shaped PbS/CdS NCs at 150 °C. (d, g) 4.3-nm PbS/CdS NCs fused at 100 °C. (e, h) 4.3-nm PbS/CdS NCs fused at 150 °C. (f, j) Fragments of the SMENA solid fabricated by fusing thick-shelled PbS/CdS NCs (4.3-nm PbS coated with 12−14 ML of CdS) at 150 °C. Epitaxial associations of neighboring CdS shells can be seen in panel f.

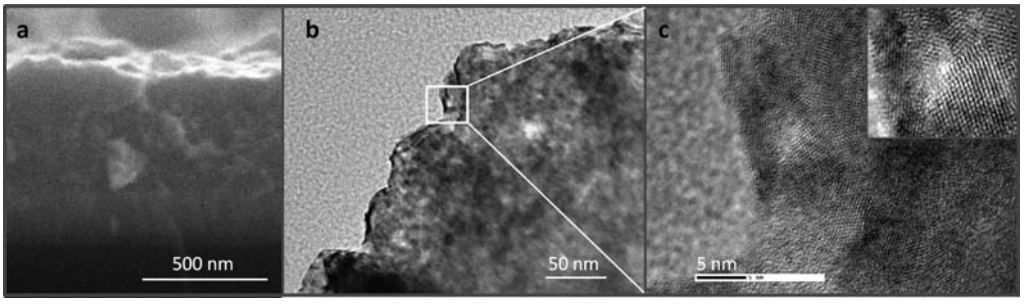

Figure 5. Electron microscopic images of the SMENA solids following the pore filling step. (a) Scanning electron microscope image of PbS/CdS films. (b) TEM image of a SMENA fragment. (c) Enlargement of the highlighted area, showing lattices fringes, which correspond to SILAR-deposited CdS.

distinguishable in the absorbance spectra (Figure 9d), indicating that the quantum confinement was partly preserved during the fusion process. These measurements agree with previous studies showing that epitaxial fusion of high-reactivity facets of NCs can occur at temperatures as low as 60−100 °C, provided that organic ligands are desorbed from NC surfaces.[86]

In order to improve the conductance of SMENA solids, trapping and scattering of carriers should be reduced to a minimum. While the shell growth and the subsequent fusion of core/shell NCs is expected to result in the formation of high-quality interfaces at PbS−CdS[82] and CdS−CdS[87] boundaries (Figures 2b and 4f, respectively), which are associated with little charge scattering, the surfaces of interfused NCs can still produce carrier traps limiting the carrier diffusion lengths. Ideally, close packing of NCs in a solid with minimal amount of exposed surfaces is desired. This scenario is realized for cubic-shaped core/shell NCs, which form closely packed nanocrystal films upon fusion (Figure 4c). Packing of round NCs, on the other hand, is less ordered and produces a significant fraction of unpassivated surface areas, at which carriers can trap and subsequently decay without reaching the opposite electrode. To passivate these surfaces, NC solids can be further treated with an additional S_2 material (CdS, ZnS), which is introduced into the pores of fused core/shell NCs via CBD or SILAR methodology. This step results in partial filling of gaps in SMENA, giving rise to monolithic solids, with identifiable CdS lattice structure (see Figure.5). The ability of Cd and S ions to penetrate through nanoparticle films has been exemplified in recent experiments on porous TiO_2 films (3−4 μm in thickness), for which CdS material is deposited throughout the entire depth of the film[88] (judging by the even coloration of both the front and back sides of the opaque Degussa TiO_2 layer on glass). Notably, filling the pores of interfused PbS/CdS core/shell NCs with additional CdS does not increase the inter-NC distance and thus does not affect the electrical coupling between nanoparticles in the film. According to Figure 3a,d, NC solids resulting from fusion and pore-filling steps contain no traces of organic material and show identifiable excitonic features of incorporated PbS NCs. On the

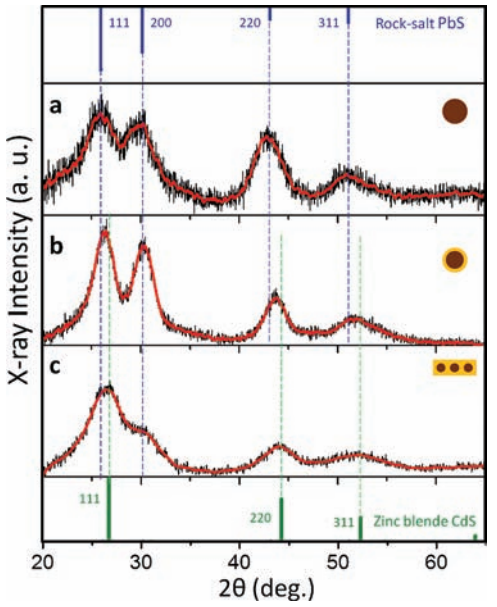

Figure 6. X-ray powder diffraction spectra of NC films corresponding to progressive stages of SMENA development. (a) XRD spectrum of 4.0-nm PbS NCs, showing characteristic Bragg peaks of rock salt PbS crystal phase. (b) XRD spectrum of fused PbS/CdS core/shell NCs. (c). XRD spectrum of CdS infilled PbS/CdS solids (seven SILAR cycles) comprising 4.0-nm PbS NC arrays.

basis of FTIR and absorbance spectra, we thus conclude that the presented strategy yields an all-inorganic encapsulation of PbS NCs exhibiting quantum confinement of electrical charges.

The structure of heterointerfaces between PbS and CdS domains was further investigated by X-ray powder diffraction (XRD). Characteristic XRD spectra in Figure 6 compare the diffraction pattern of the three samples: (a) OA-capped PbS NCs, (b) fused PbS/CdS core/shell NC films annealed at 150 °C, and (c) PbS/CdS solids after the CBD pore-filling step. According to Figure 6a, the Bragg lines corresponding to pure PbS NC powder closely match the PbS rock salt structure, as indicated by the set of blue tick marks. Growth of the 0.4-nm CdS shell onto PbS NCs produces the second set of Bragg lines matching the zinc blende phase of the CdS lattice (denoted by green tick marks). The absence of an alloying effect (generally manifested by broadening of Bragg peaks)[89] and the low density of irregularities along material boundaries observed in HR-TEM images of PbS/CdS NCs were interpreted as evidence of quasi-epitaxial bonding between PbS and CdS lattices. Upon filling the pores of PbS/CdS films with additional CdS semiconductor deposited in seven SILAR cycles, the diffraction pattern of resulting PbS/CdS solids shifted further toward higher angles (Figure 6c), indicating an increase in the volume fraction of CdS material. An apparent widening of Bragg lines in this case was attributed to unresolved contributions from PbS rock salt and CdS zinc blende crystal phases.

Improving the thermal stability of NC films is of central importance to their deployment in device applications. In organically interlinked NC arrays, a complete thermal sintering occurs at relatively low temperatures ($T \approx 150-170$ °C).[90] In the case of SMENA solids, the presence of the matrix semiconductor on NC surfaces is expected to prevent the early oxidation process, such that the thermal degradation of NCs is expected to occur at higher temperatures via phase transition of the lattice.

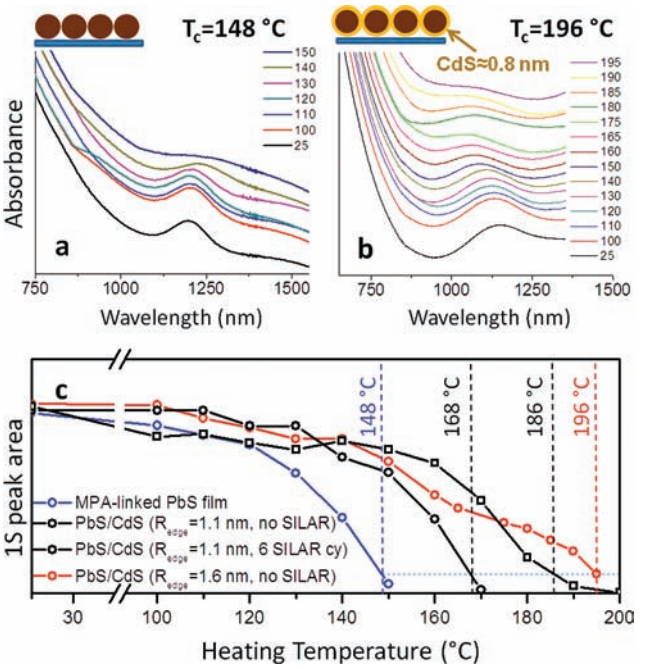

Figure 7. Comparison of thermal stability of (a) MPA-linked and (b) CdS-encapsulated PbS NC arrays, and (c) temperature dependence of the 1S peak area. R_{edge} is defined as the closest edge-to-edge distance between adjacent PbS NCs in the matrix, which is calculated as twice the thickness of the CdS shell.

Here, we test this hypothesis by comparing the thermal stability of PbS NCs incorporated into CdS matrices with that of organically interlinked PbS NC films. To this end, the effect of the substrate temperature on area of the 1S(e)−1S(h) absorption peak in both films was investigated. According to Figure 7, heating of (a) MPA-interlinked and (b) CdS-encapsulated PbS NC films in inert atmosphere results in eventual bleaching of the 1S(e)−1S(h) exciton peak, which was taken as a sintering point of PbS NCs. In the case of PbS films encapsulated with ≈0.8 nm of CdS shell, the sintering temperature was roughly 50 °C above that of MPA-interlinked PbS NC arrays, while for PbS NCs capped with 1.4 nm of CdS, the temperature difference, T_C(PbS/CdS) − T_C(PbS_{MPA}), reached 80 °C. In both cases, SMENA films were not treated with an additional CdS (pore-filling step), such that the observed enhancement in the thermal stability of PbS NCs incorporated into SMENA solids was attributed solely to the existence of the CdS shell. Upon filling of the SMENA pores with additional CdS (six SILAR cycles) in films with CdS shell of 0.55 nm (R_{edge} = 1.1 nm), the sintering temperature was increased by an additional 18 °C, as evident from the comparison of curves (○, no SILAR; □, six cycles of SILAR) in Figure 7. Evolution of the absorption spectra for the latter film is shown in Figure SF3 (Supporting Information). Overall, the above experiments confirm that matrix encapsulation of NC array results in an enhanced heat resistance of incorporated NCs as compared to organically interlinked NC solids.

In addition to the observed increase in the thermal threshold for sintering, the shape of PbS NCs capped with CdS appeared to evolve differently with increasing temperature than that of MPA-linked solids. As seen in Figure 7a, heating of organically passivated PbS NCs resulted in a progressive red-shifting of the exciton absorption peak, while CdS-capped PbS (Figure 7b) underwent an initial blue shift followed by an eventual red-shift at

T = 170−175 °C. A similar trend was observed for pore-filled SMENA films, the absorbance changes of which are shown in Figure SF3 (Supporting Information). The difference in the evolution of absorbance spectra for the two types of films is attributed to the fact that heating of MPA-linked NCs promotes ligand desorption and subsequent clustering of neighboring PbS nanoparticles, as evident by the decrease in the confinement length and associated red shift of the absorbance peak starting at $T \approx 100$ °C; meanwhile, thermal sintering of PbS/CdS SMENA preserves the same length of quantum confinement throughout the 25−170 °C range, causing some shrinking of PbS cores due to allowing of the PbS/CdS interface (as manifested by a blue shift of the exciton peak), before sintering-induced red-shifting becomes dominant at higher temperatures (T > 170 °C). This is an important result, indicating that the initial sintering in CdS-capped PbS NC arrays occurs via alloying of the PbS/CdS interface and not through clustering of PbS NCs.

One key parameter that determines the macroscopic properties of NC solids is the degree of coupling between electrical charges in the film.[74] When electronic states of neighboring NCs are strongly coupled, the associated charge carrier wave functions delocalize over the entire NC array. This creates conduction channels for electrons and holes to move freely, much like it happens in an ordinary crystalline solid. These films are thus best suited for applications requiring the transport of charges, which include solar cells, photodetectors, and FETs. Conversely, in films with weakly coupled NCs, the site localization of excited carriers suppresses the transport of charges across the solid, turning the film insulating. The existence of large potential barriers between NCs in this case enables the radiative decay of excitons, which can find potential use in such applications as lasers, waveguides, and LEDs.

Theoretically, the energy of internanocrystal coupling in a film can be expressed within the Wentzel−Kramers−Brillouin (WKB) approximation as[91]

$$\beta \approx h\nu \exp[-2(2m^*\Delta E/\hbar^2)^{1/2}R_{edge}] \quad (1)$$

where ν is a constant with units of frequency, m^* is the carrier effective mass, and R_{edge} is the shortest edge-to-edge distance between the adjacent NCs in the film. This fairly simple approach takes into account only the resonant tunneling mechanism of charge coupling between adjacent nanocrystals and does not include the effects of disorder or level-broadening in the system. The magnitude of the energy term in eq 1 determines the type of charge coupling in NC films, which is inferred from the ratio of the coupling energy (β) to the charging energy (E_c), defined as the energy required for adding an extra charge to a NC,[92] as well as the ratio of β to the room-temperature k_BT. Since, for most NC films, E_c is greater than k_BT (at T = 30 °C), one can define three distinct regimes of charge localization in NC solids. First, when $\beta < k_BT$ carriers, are strongly localized, such that the resulting NC film is essentially insulating. In this case, the charge transport can occur only through tunneling. In the regime when $k_BT < \beta < E_c$, carrier wave functions overlap across domains of several NCs but the states are still separated by the Coulomb gap.[93] In the third regime, when $\beta > E_c$, also known as the Mott metal−insulator transition (MIT),[92,94] wave functions become delocalized throughout the entire solid, such that the film properties start to resemble those of crystalline bulk materials.

Here we estimate the nature of electric coupling in fabricated SMENA solids by modeling the electron coupling energy as a function of inter-NC separation (R_{edge}) for the three SMENA systems: 4-nm PbS NCs in a CdS matrix, 6-nm PbS in a CdS matrix, and 4-nm PbS in a ZnS matrix. Figure 8a shows a relative alignment of band edges for these heteronanomaterials, which was partly confirmed in this work through the observation of the characteristic optical properties (e.g., Figure 2d). According to the energy diagram, the strongest localization of electrons is expected to occur in a PbS/ZnS system, while 4-nm PbS NC arrays encased within a CdS matrix should exhibit the highest degree of state delocalization. Notably, when the diameter of PbS is less than 4 nm, the PbS/CdS NCs could transition into a quasi type II heterostructure.[95−97] In such nanoparticles, electrons are delocalized over the entire volume of the solid, causing the loss of quantum confinement in the system. While this type of NC coupling constitutes an interesting case of bulklike NC solids, the present experiments are mainly focused on systems for which a nonvanishing inter-NC potential barrier still exists, such that the energies of excited states could be tuned via the nanoparticle size.

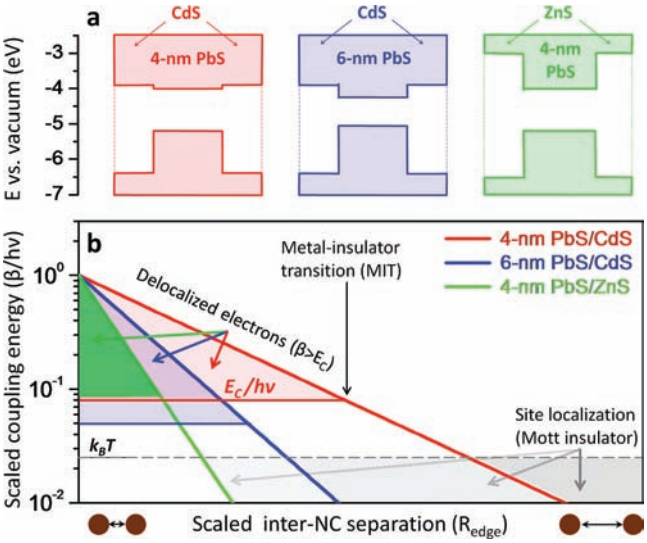

Figure 8. (a) Energy diagram showing relative alignment of conduction and valence band edges at heterointerfaces of three NC/matrix combinations: 4.0-nm PbS/CdS, 6.0-nm PbS/CdS, and 4.0-nm PbS/ZnS, representing the cases of delocalized, domain-localized, and site-localized 1S(e) wave functions, respectively. (b) Dependence of coupling energy (β) on inter-NC distance (R_{edge}) for the three material systems shown in panel a. The colored areas (red, blue, and green) indicate the regime of delocalized electrons, while gray-shaded areas highlight the regime of strongly localized charges.

The results of model calculations are summarized in Figure 8b. For each of the investigated material systems, we identify three coupling regimes, denoted as (1) delocalized electrons (colored areas, $\beta > E_c$), (2) domain-localized electrons or tunneling coupling regime ($k_BT < \beta < E_c$), and (3) site-localized electrons or Mott insulator regime (gray shading, $\beta < k_BT$). The R_{edge} parameter is calculated in relative units of length, which preserve the correct length ratio of MIT to Mott transitions between the three investigated SMENA systems. For instance, according to Figure 8b, the same inter-NC separation, R_{edge}, turns 4-nm PbS/CdS solids conductive, while rendering 4-nm PbS/ZnS films insulating. These calculations also indicate that the value of R_{edge} associated with the MIT transition in 4-nm PbS/CdS solids is 1.5 times greater than that of 6-nm PbS/CdS and 3.1 times greater than that of 4-nm PbS/ZnS solids.

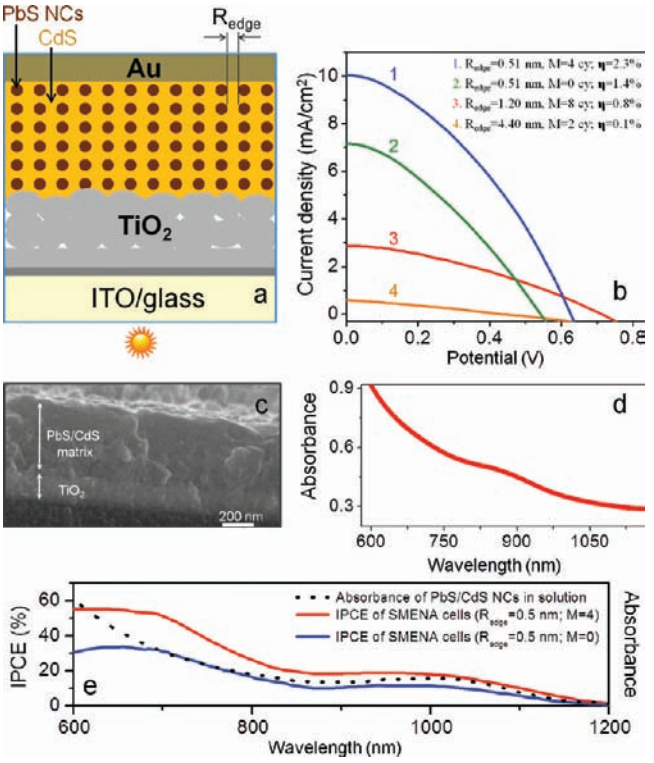

Figure 9. (a) Schematic of the depleted heterojunction solar cell comprising an FTO/glass working electrode, 200−400 nm TiO_2 layer, PbS/CdS SMENA layers (~250−400 nm), and a Au/Pd counter-electrode (not visible). (b) Best J-V outputs of the four types of PbS/CdS solar cell: (1) 3.1-nm PbS/CdS (R_{edge} = 0.51 nm, four SILAR cycles), (2) 3.1-nm PbS/CdS (R_{edge} = 0.51 nm, zero SILAR cycles), (3) 3.2-nm PbS/CdS (R_{edge} = 1.2 nm, eight SILAR cycles) and (4) 3.2-nm PbS/CdS (R_{edge} = 4.4 nm, two SILAR cycles) (c) Cross-sectional SEM image of the NC film on TiO_2, prepared through the crystallographic fusion of 3.2-nm PbS/1.5 ML CdS core/shell NCs, followed by the CdS pore-infilling step (eight cycles). (d) Representative absorbance spectrum of a SMENA cell on FTO glass. (e) IPCE spectra of the two SMENA cells, the $J-V$ outputs of which are marked 1 and 2 in panel b.

The predicted regimes of NC coupling are in line with the experimental results obtained for the two types of NC solids, representing the cases of highly delocalized and strongly insulating films. The former was fabricated by incorporating ≈3.8-nm PbS NCs into a CdS matrix, such that the inter-NC spacing, R_{edge}, was 0.7 nm (1S exciton feature at λ = 1070 nm). For these solids, the OA → MPA ligand exchange step quenched most of the original PbS band-edge fluorescence, indicating the onset of strong coupling even in the presence of short-chain ligands on PbS surfaces. The subsequent crystallographic fusion of the respective shells resulted in the complete suppression of fluorescence and simultaneous widening of the exciton absorption peak, which was interpreted as evidence of further delocalization of 1S electrons. The presence of characteristic quantum confinement features in the absorbance spectra of annealed NC films (Figure 9d), however, indicated that the regime of strong delocalization (regime 1) was not reached for R_{edge} = 0.7 nm. Only by decreasing R_{edge} in PbS/CdS solids to less than 0.5 nm were we able to reach the regime of strong coupling, characterized by a significant widening of the 1S exciton absorbance. The conductance of 3.8-nm PbS/CdS films, with an expected domain localization of NC charges, was found to be comparable to that of MPA-linked solids, as was attested by similar performances of CdS-encapsulated (Figure 9b) and MPA-linked (Figure SF5, Supporting Information) PbS films in prototype solar cells.

To fabricate NC solids showing strong localization of charges (regime 3), 3.0-nm PbS NCs were coated with 2.4 nm of CdS shell followed by 0.4 nm of ZnS shell. In this case, the direct deposition of more than 1 ML of ZnS onto PbS NCs did not result in the formation of a uniform shell, possibly due to a significant mismatch of lattice constants for these semiconductors (strain ≈8.2%). The employment of a CdS intermediate layer facilitated a gradual relief of the lattice stress and allowed deposition of 0.4 nm of ZnS [R_{edge} = 2(0.4 + 2.4) nm = 5.6 nm]. The resulting PbS/CdS/ZnS NCs solids were developed on top of FTO glass (sufficient surface roughness was required for the films to adhere to the substrate) by fusing MPA-capped NCs at 150 °C, followed by the ZnS pore-infilling step. According to Figure SF4 (Supporting Information), the band edge emission of all-inorganic PbS/CdS/ZnS solids was still distinguishable after the annealing step, indicating a strong localization of both carriers at PbS sites. The insulating character of these films was confirmed in photocurrent measurements, for which the resulting current density did not exceed 0.01 mA/cm^2 at AM1.5 illumination.

The photovoltaic characteristics of SMENA films were investigated by the use of a depleted heterojunction (DH) solar cell architecture,[64] schematically illustrated in Figure 9a. In comparison with a commonly used Schottky barrier NC cell,[84] where the p−n junction is formed at the metal−electrode interface, the DH architecture relies on a heterojunction of the two semiconductors to separate charges between FTO and Au electrodes. This design feature allows increasing an open circuit voltage of the device (V_{os}), which is explained by the fact that the Fermi level of the metal electrode is no longer pinned by the defect states at the semiconductor−metal interface.[73] In addition, the DH cell design relies on the incorporated TiO_2 layer to block photoinduced holes from the working electrode. This increases the shunt resistance of the cell, resulting in a greater fill factor (FF) of the device.

To fabricate a prototype DH cell, SMENA solids were developed on top of a TiO_2 film and then capped with 20−60 nm Au/Pd electrodes. A TiO_2 film was spin-coated from DyeSol nanoparticle precursor on FTO-coated glass (resistance = 12 Ω/sq) and subsequently annealed at 450−480 °C to remove organic traces (see Experimental Section). The thickness of the resulting layer of TiO_2 ranged from 200 to 400 nm, as was estimated from SEM measurements. To develop the light-absorbing layer, PbS/CdS core/shell NCs capped with original OA ligands were spin-coated onto TiO_2 layer via 8−10 LbL cycles, totaling 350−400 nm. The film was heated to 150−160 °C for ~15 min after every three cycles. Upon deposition of the NC layer, the pores of the resulting solid were further filled with additional CdS (2−10 SILAR cycles), and the film was capped with Au/Pd electrodes through a shadow mask. The area of each metal pixel was roughly 0.03 cm^2. To improve the quality of deposited NC films, a modified spin-coating methodology comprising both soaking and spinning cycles was developed (see Experimental Section). Without the use of such prolonged soaking (1 min) prior to spin-coating, the quality of the resulting films was generally poor, as was identified by low surface reflectivity and a large density of pinholes.

Figure 9b shows the set of best $J-V$ measurements of the four types of PbS/CdS solar cells (FTO/TiO_2/SMENA/Au/Pd),

representing different combinations of the inter-NC separation (R_{edge}) and the number of infilling SILAR cycles (denoted as M in the figure). The highest PCE value under AM1.5 illumination (η = 2.3%; FF = 0.38) was realized for the cells fabricated with four CdS infilling cycles (M = 4) and R_{edge} of 0.5 nm; meanwhile, the use of eight infilling cycles and R_{edge} of 1.2 nm produced lower PCE (<0.8%) but consistently yielded large values of the open circuit voltage (V_{OC} > 0.72 V). The relatively low value of the cell fill factor was attributed to a high in-series resistance of the device, which could be related to charge trapping on remaining dangling bonds in the system. This hypothesis was supported by the fact that for SMENA cells where pores were not filled with CdS (but were terminated with either $ZnCl_2$ or CTAB), the best efficiency was limited to η = 1.38% (Figure 9b, green curve). The increase in R_{edge} from 0.5 to 4.4 nm (Figure 9b, orange curve) was accompanied by a significant drop in the cell efficiency to less than 0.1% and was attributed to the onset of carrier localization (see Figure 8, red curve). For best-performing cells ($R_{edge} \approx 0.5-0.6$ nm, M > 2 cycles), the typical range of cell efficiencies was η = 1.5−2.3%, where η is the PCE of the best-performing pixel (out of 16) in a cell. For high-quality films (as characterized by their smooth, reflective appearance and even coloration of the NC layer), about half of all pixels showed efficiencies within 60% of the best-performing pixel. On the basis of the absorbance profile of a typical SMENA solar cell (Figure 9d) showing a distinguishable exciton feature, we infer that carriers in the film show some degree of domain localization. Overall, the observed range of PCE values for SMENA devices was somewhat lower than those of the best reported NC solar cells,[64,98,99] for which η can reach 6%. The SMENA cells stored in ambient conditions (open to air and moisture) for up to 3 months showed 20−30% reduction in the performance, which is on the par with the stability of EDT-interlinked PbS solar cells reported in ref 100. The primary causes of SMENA cell degradation were not clear and could be related to physical damage of the 30-nm Au/Pd contact resulting from multiple applications of the spring-loaded probe tip. We also note that only a minimal optimization of the cell performance was undertaken in the course of this study, and future work will be needed to address the effect of the film morphology (R_{edge}, NC diameter, matrix material) on the cell efficiency.

The light-harvesting characteristics of SMENA cells are summarized in Figure 9e, showing incident photon to electron conversion efficiency (IPCE) profiles and optical absorbance of the two types of SMENA cells corresponding to the two best $J-V$ outputs in Figure 9b (marked as 1 and 2). The IPCE of the 2.3% cell (R_{edge}= 0.5 nm, M = 4 cycles) reveals a distinguishable contribution from PbS NCs into the observed photocurrent, as manifested by the identifiable 1S exciton feature in the IPCE spectrum. The IPCE profile of the second cell prepared with zero CdS infilling cycles (M = 0) shows a similar profile, where the amplitude is proportionally decreased compared to that of CdS-treated film. The lower value of the photocurrent in this case is attributed to higher rate of charge trapping on surfaces of interfused PbS/CdS NCs, resulting from the diminished potential barrier between 1S carriers in PbS and the surfaces of CdS. The contribution of the CdS matrix into the photocurrent could not be evaluated in these measurements due to spectral limitations of the IPCE collection system. Nevertheless, as indirect evidence of nonvanishing effect of the CdS material on photocurrent, the $J-V$ output of cell 4 in Figure 9b (for which the CdS-to-PbS volume ratio was substantial) yielded high values of V_{OC} (>0.7 V), consistent with the CdS band gap value.

In conclusion, a novel strategy for assembling semiconductor nanocrystals into all-inorganic solids is presented. The reported methodology is designed to overcome the key limitations of the "cross-linking" approach to assembly of NC films, associated with poor thermal and chemical stability of the ligand−nanocrystal system, by encasing nanocrystal arrays into a matrix of a wide band gap semiconductor. Here, we employ CdS and ZnS matrices to encapsulate PbS NC arrays, such that the quantum confinement of incorporated nanocrystals is partly preserved and can be controlled by tuning the inter-NC separation in the film. Fabricated films exhibit good thermal stability, which is attributed to the heteroepitaxial structure of nanocrystal−matrix interfaces, and show compelling light-harvesting performance in prototype solar cells. Model calculations have been performed to evaluate the effect of inter-NC separation in the film on the degree of electrical coupling between adjacent NCs in the solid. The results of these calculations were supported by experiments performed on ZnS- and CdS-encapsulated NC arrays. It is expected that the matrix-encapsulation approach could be extended to other type I semiconductor/matrix combinations to aid the "bottom-up" development of all-inorganic NC films showing high carrier mobility, quantum confinement of incorporated charges, and compelling air stability.

■ ASSOCIATED CONTENT

Supporting Information. Experimental details and five figures with additional TEM and HRTEM images. This material is available free of charge via the Internet at http://pubs.acs.org.

■ AUTHOR INFORMATION

Corresponding Author
zamkovm@bgsu.edu

Author Contributions
[§]These authors contributed equally to this work.

■ ACKNOWLEDGMENT

We acknowledge OBOR "Material Networks" program and Bowling Green State University for financial support. This work was partly supported by the NSF under Award CHE-1112227. We thank N. R. Neal for valuable discussions related to solar cell development.

■ REFERENCES

(1) Klimov, V. I.; Mikhailovsky, A. A.; Xu, S.; Malko, A.; Hollingsworth, J. A.; Leatherdale, C. A.; Eisler, H.; Bawendi, E. H. *Science* **2000**, *290*, 314–317.
(2) Klimov, V. I. *J. Phys. Chem. B* **2006**, *110*, 16827–16845.
(3) Klimov, V. I.; Ivanov, S. A.; Nanda, J.; Achermann, M.; Bezel, I.; McGuire, J. A.; Piryatinski, A. *Nature* **2007**, *447*, 441–446.
(4) Hillhouse, H. W.; Beard, M. C. *Curr. Opin. Colloid Interface Sci.* **2009**, *14*, 245–259.
(5) Huynh, W. U.; Dittmer, J. J.; Alivisatos, A. P. *Science* **2002**, *295*, 2425–2427.
(6) McDonald, S. A.; Konstantatos, G.; Zhang, S.; Cyr, P. W.; Klem, E. J. D.; Levina, L.; Sargent, E. H. *Nat. Mater.* **2005**, *4*, 138–142.
(7) Ellingson, R. J.; Beard, C. M.; Johnson, J. C.; Yu, P.; Micic, O. I.; Nozik, A. J.; Shabaev, A.; Efros, A. L. *Nano Lett.* **2005**, *5*, 865–871.
(8) Maria, A.; Cyr, P. W.; Klern, E. J. D.; Levina, L.; Sargent, E. H. *Appl. Phys. Lett.* **2005**, *87*, No. 213112.

(9) Kim, S. J.; Kim, W. J.; Cartwright, A. N.; Prasad, P. N. *Appl. Phys. Lett.* **2008**, *92*, No. 191107.
(10) Gur, I.; Fromer, N. A.; Geier, M. L.; Alivisatos, A. P. *Science* **2005**, *310*, 462–465.
(11) Guo, Q.; Kim, S. J.; Kar, M.; Shafarman, W. N.; Birkmire, R. W.; Stach, E. A.; Agrawal, R.; Hillhouse, H. W. *Nano Lett.* **2008**, *8*, 2982–2987.
(12) Leschkies, K. S.; Beatty, T. J.; Kang, M. S.; Norris, D. J.; Aydil, E. S. *ACS Nano* **2009**, *3*, 3638–3648.
(13) Ma, W.; Luther, J. M.; Zheng, H.; Wu, Y.; Alivisatos, A. P. *Nano Lett.* **2009**, *9*, 1699–1703.
(14) Lee, H. J.; Yum, J.-H.; Leventis, H. C.; Zakeeruddin, S. M.; Haque, S. A.; Chen, P.; Seok, S. I.; Grätzel, M.; Nazeeruddin, M. K. *J. Phys. Chem. C* **2008**, *112*, 11600–11608.
(15) Riha, S. C.; Fredrick, S. J.; Sambur, J. B.; Liu, Y.; Prieto, A. L.; Parkinson, B. A. *ACS Appl. Mater. Interfaces* **2011**, *3*, 58–66.
(16) Hao, E.; Yang, B.; Zhang, J. H.; Zhang, X.; Sun, J.; Shen, S. *J. Mater. Chem.* **1998**, *8*, 1327–1328.
(17) Mora-Sero, I.; Bisquert, J.; Dittrich, T.; Belaidi, A.; Susha, A. S.; Rogach, A. L. *J. Phys. Chem. C* **2007**, *111*, 14889–14892.
(18) Yu, P. R.; Zhu, K.; Norman, A. G.; Ferrere, S.; Frank, A. J.; Nozik, A. J. *J. Phys. Chem. B* **2006**, *110*, 25451–25454.
(19) Vogel, R.; Hoyer, P.; Weller, H. *J. Phys. Chem.* **1994**, *98*, 3183.
(20) Hoyer, P.; Konenkamp, R. *Appl. Phys. Lett.* **1995**, *66*, 349–351.
(21) Lee, H.; Leventis, H. C.; Moon, S. J.; Chen, P.; Ito, S.; Haque, S. A.; Torres, T.; Nüesch, F.; Geiger, T.; Zakeeruddin, S. M.; Gratzel, M.; Nazeerruddin, M. K. *Adv. Funct. Mater.* **2009**, *19*, 2735–2742.
(22) Lee, H.; Wang, M.; Chen, P.; Gamelin, D. R.; Zakeeruddin, S. M.; Grätzel, M.; Nazeeruddin, M. K. *Nano Lett.* **2009**, *9*, 4221–4227.
(23) Acharya, K. P.; Hewa-Kasakarage, N. N.; Alabi, T. R.; Nemitz, I.; Khon, E.; Ullrich, B.; Anzenbacher, P.; Zamkov, M. *J.Phys. Chem. C* **2010**, *114*, 12496.
(24) Acharya, K. P.; Hewa-Kasakarage, N. N.; Khon, E.; Khnayzer, R. S.; O'Conner, T.; Nemitz, I.; Klinkova, A.; Anzenbacher, P.; Zamkov, M. *ACS Nano* **2011**, *5*, 4953.
(25) Wang, Q.; Zhu, K.; Neale, N. R.; Frank, A. J. *Nano Lett.* **2009**, *9*, 806–813.
(26) Oregan, B.; Grätzel, M. *Nature* **1991**, *353*, 737–740.
(27) Kamat, P. V.; Flumiani, M.; Dawson, A. *Colloids Surf. A* **2002**, *202*, 269–279.
(28) Dawson, A.; Kamat, P. V. *J. Phys. Chem. B* **2001**, *105*, 960–966.
(29) Borensztein, Y.; Delannoy, L.; Djedidi, A.; Barrera, R. G.; Louis, C. *J. Phys. Chem. C* **2010**, *114*, 9008.
(30) Acharya, K. P.; Khnayzer, R. S.; O'Connor, T.; Diederich, G.; Kirsanova, M.; Klinkova, A.; Roth, D.; Kinder, E.; Imboden, M.; Zamkov, M. *Nano Lett.* **2011**, *11*, 2919.
(31) Amirav, L.; Alivisatos, A. P. *J. Phys. Chem. Lett.* **2010**, *1*, 1051–1054.
(32) Coe, S.; Woo, W. K.; Bawendi, M.; Bulovic, V. *Nature* **2002**, *420*, 800–803.
(33) Tessler, N.; Medvedev, V.; Kazes, M.; Kan, S. H.; Banin, U. *Science* **2002**, *295*, 1506–1508.
(34) Steckel, J. S.; Snee, P.; Coe-Sullivan, S.; Zimmer, J. R.; Halpert, J. E.; Anikeeva, P.; Kim, L. A.; Bulovic, V.; Bawendi, M. G. *Angew Chem., Int. Ed.* **2006**, *45*, 5796–5799.
(35) Colvin, V. L.; Schlamp, M. C.; Alivisatos, A. P. *Nature* **1994**, *370*, 354–357.
(36) Schlamp, M. C.; Peng, X. G.; Alivisatos, A. P. *J. Appl. Phys.* **1997**, *82*, 5837–5842.
(37) Mattoussi, H.; Radzilowski, L. H.; Dabbousi, B. O.; Thomas, E. L.; Bawendi, M. G.; Rubner, M. F. *J. Appl. Phys.* **1998**, *83*, 7965–7974.
(38) Sun, Q.; Wang, A. Y.; Li, L. S.; Wang, D.; Zhu, T.; Xu, J.; Yang, C.; Li, Y. *Nat. Photonics* **2007**, *1*, 717–722.
(39) Caruge, J. M.; Halpert, J. E.; Wood, V.; Bulovic, V.; Bawendi, M. G. *Nat. Photonics* **2008**, *2*, 247–250.
(40) Medintz, I. L.; Uyeda, H. T.; Goldman, E. R.; Mattoussi, H. *Nat. Mater.* **2005**, *4*, 435–446.
(41) Bruchez, M.; Moronne, M.; Gin, P.; Weiss, S.; Alivisatos, A. P. *Science* **1998**, *281*, 2013–2016.
(42) Mattoussi, H.; Mauro, J. M.; Goldman, E. R.; Anderson, G. P.; Sundar, V. C.; Mikulec, F. V.; Bawendi, M. G. *J. Am. Chem. Soc.* **2000**, *122*, 12142–12150.
(43) Wang, R. Y.; Feser, J. P.; Lee, J. S.; Talapin, D. V.; Segalman, R.; Majumdar, A. *Nano Lett.* **2008**, *8*, 2283–2288.
(44) Kovalenko, M. V.; Scheele, M.; Talapin, D. V. *Science* **2009**, *324*, 1417–1420.
(45) Ridley, B. A.; Nivi, B.; Jacobson, J. M. *Science* **1999**, *286*, 746–749.
(46) Lee, S.; Jeong, S.; Kim, D.; Park, B. K.; Moon, J. *J. Superlattices Microstruct.* **2007**, *42*, 361–368.
(47) Schneider, J. J.; Hoffmann, R. C.; Engstler, J.; Soffke, O.; Jaegermann, W.; Issanin, A.; Klyszcz, A. A. *Adv. Mater.* **2008**, *20*, 3383–3387.
(48) Talapin, D. V.; Mekis, l.; Gotzinger, S.; Kornowski, A.; Benson, O.; Weller, H. *J. Phys. Chem. B* **2004**, *108*, 18826–18831.
(49) Talapin, D. V.; Murray, C. B. *Science* **2005**, *310*, 86–89.
(50) Lee, J. S.; Shevchenko, E. V.; Talapin, D. V. *J. Am. Chem. Soc.* **2008**, *130*, 9673–9675.
(51) Erwin, S. C.; Zu, L. J.; Haftel, M. I.; Efros, A. L.; Kennedy, T. A.; Norris, D. J. *Nature* **2005**, *436*, 91–94.
(52) Salgueirino-Maceira, V.; Correa-Duarte, M. A. *Adv. Mater.* **2007**, *19*, 4131.
(53) Son, D. I.; Kim, J. H.; Park, D. H.; Choi, W. K.; Li, F.; Ham, J. H.; Kim, T. W. *Nanotechnology* **2008**, *19*, No. 055204.
(54) Liz-Marzan, L. M.; Mulvaney, P. *J. Phys. Chem. B* **2003**, *107*, 7312–7326.
(55) Das, B. C.; Batabyal, S. K.; Pal, A. J. *Adv. Mater.* **2007**, *19*, 4172–4176.
(56) Das, B. C.; Pal, A. J. *Small* **2008**, *4*, 542–547.
(57) Ghosh, B.; Sahu, S.; Pal, A. J. *J. Phys. Chem. C* **2008**, *112*, 11290–11294.
(58) Katari, J. E. B.; Colvin, V. L.; Alivisatos, A. P. *J. Phys. Chem.* **1994**, *98*, 4109.
(59) Brust, M.; Bethell, D.; Schiffrin, D. J.; Kiely, C. J. *J. Adv. Mater.* **1995**, *7*, 795.
(60) Muller, K. H.; Wei, G.; Raguse, B.; Myers, J. J. *Phys. Rev. B* **2003**, *68*, No. 155407.
(61) Klem, E. J. D.; MacNeil, D. D.; Cyr, P. W.; Levina, L.; Sargent, E. H. *Appl. Phys. Lett.* **2007**, *90*, No. 183113.
(62) Clifford, J. P.; Konstantatos, G.; Johnston, K. W.; Hoogland, S.; Levina, L.; Sargent, E. H. *Nat. Nanotechnol.* **2009**, *4*, 40.
(63) Murphy, J. E.; Beard, M. C.; Nozik, A. J. *J. Phys. Chem. B* **2006**, *110*, 25455.
(64) Pattantyus-Abraham, A. G.; Kramer, I. J.; Barkhouse, A. R.; Wang, X.; Konstantatos, G.; Debnath, R.; Levina, L.; Raabe, I.; Nazeeruddin, M. K.; Gratzel, M.; Sargent, E. H. *ACS Nano* **2010**, *4*, 3374–3380.
(65) Murray, C. B.; Norris, D. J.; Bawendi, M. G. *J. Am. Chem. Soc.* **1993**, *115*, 8706.
(66) Yu, D.; Wang, C.; Guyot-Sionnest, P. *Science* **2003**, *300*, 1277.
(67) Kovalenko, M. V.; Bodnarchuk, M. I.; Zaumseil, J.; Lee, J. S.; Talapin, D. V. *J. Am. Chem. Soc.* **2010**, *132*, 10085–10092.
(68) Liu, Y.; Gibbs, M.; Puthussery, J.; Gaik, S.; Ihly, R.; Hillhouse, H. W.; Law, M. *Nano Lett.* **2010**, *10*, 1960–1969.
(69) Tang, J.; Kemp, K. W.; Hoogland, S.; Jeong, K. S.; Liu, H.; Levina, L.; Furukawa, M.; Wang, X.; Debnath, R.; Cha, D.; Chou, K. W.; Fischer, A.; Amassian, Ar.; Asbury, J. B.; Sargent, E. H. *Nat. Mater.* **2011**, *10*, 765–771.
(70) Liu, Y.; Gibbs, M.; Perkins, C. L.; Tolentino, J.; Zarghami, M. H.; Bustamante, J., Jr.; Law, M. *Nano Lett.* **2011**, ASAP (DOI: 10.1021/nl2028848.
(71) Rauch, T.; Boberl, M.; Tedde, S. F.; Furst, J.; Kovalenko, M. V.; Hesser, G.; Lemmer, U.; Heiss, W.; Hayden, O. *Nat. Photonics* **2009**, *3*, 332.
(72) Hoth, C. N.; Choulis, S. A.; Schilinsky, P.; Brabec, C. J. *Adv. Mater.* **2007**, *19*, 3973.
(73) Tang, J.; Sargent, E. H. *Adv. Mater.* **2011**, *23*, 12–29.
(74) Talapin, D. V.; Lee, J. S.; Kovalenko, M. V.; Shevchenko, E. V. *Chem. Rev.* **2010**, *110*, 389.

(75) Jones, M.; Lo, S. S.; Scholes, G. D. *Proc. Natl. Acad. Sci. U.S.A.* **2009**, *106*, 3011–3016.
(76) Lingley, Z; Lu, S.; Madhukar, A. *Nano Lett.* **2011**, *11*, 2887–2891.
(77) Pathan, H. M.; Lokhande, C. D. *Bull. Mater. Sci.* **2004**, *27*, 85.
(78) Zabet-Khosousi, A.; Dhirani, A. A. *Chem. Rev.* **2008**, *108*, 4072.
(79) Hines, M. A.; Scholes, G. D. *Adv. Mater.* **2003**, *15*, 1844–1849.
(80) Pietryga, J. M.; Werder, D. J.; Williams, D. J.; Casson, J. L.; Schaller, R. D.; Klimov, V. I. *J. Am. Chem. Soc.* **2008**, *130*, 4879–4885.
(81) Rogach, A. L.; Eychmuller, A.; Hickey, S. G.; Kershaw, S. V. *Small* **2007**, *3*, 536–557.
(82) Pietryga, J. M.; Werder, D. J.; Williams, D. J.; Casson, J. L.; Schaller, R. D.; Klimov, V. I.; Hollingsworth, J. A. *J. Am. Chem. Soc.* **2008**, *130*, 4879–4885.
(83) Neo, M. S.; Venkatram, N.; Li, G. S.; Chin, W. S.; Ji, W. *J. Phys. Chem. C* **2010**, *114*, 18037–18044.
(84) Luther, J. M.; Law, M.; Beard, M. C.; Song, Q.; Reese, M. O.; Ellingson, R. J.; Nozik, A. J. *Nano Lett.* **2008**, *8*, 3488.
(85) Zarghami, M. H.; Liu, Y.; Gibbs, M.; Gebremichael, E.; Webster, C.; Law, M. *ACS Nano* **2010**, *4*, 2475–2485.
(86) Hanrath, T.; Veldman, D.; Choi, J. J.; Christova, C. G.; Wienk, M. M.; Janssen, R. A. J. *ACS Appl. Mater. Interfaces* **2009**, *1*, 244–250.
(87) Li, Z. G.; Sui, J.; Li, X.; Cai, W. *Langmuir* **2011**, *27*, 2258–2264.
(88) Acharya, P.; Khatri, H.; Marsillac, S.; Ullrich, B.; Anzenbacher, P.; Zamkov, M. *Appl. Phys. Lett.* **2010**, *97*, No. 201108.
(89) Gurusinghe, P. G.; Hewa-Kasakarage, N. N.; Zamkov, M. *J. Phys. Chem. C* **2008**, *112*, 12795.
(90) Goodfellow, B. W.; Patel, R. N.; Panthani, M. G.; Smilgies, D. M.; Korgel, B. A. *J. Phys. Chem. C* **2011**, *115*, 6397–6404.
(91) Chandler, R. E.; Houtepen, A. J.; Nelson, J.; Vanmaekelbergh, D. *Phys. Rev. B* **2007**, *75*, No. 085325.
(92) Remacle, F.; Levine, R. D. *ChemPhysChem* **2001**, *114*, 10239.
(93) Beloborodov, I. S.; Lopatin, A. V.; Vinokur, V. M.; Efetov, K. B. *Rev. Mod. Phys.* **2007**, *79*, 469.
(94) Mott, N. *Conduction in Non-Crystalline Materials*, 2nd ed.; Clarendon Press: Oxford, U.K., 1993.
(95) Nemchinov, A.; Kirsanova, M.; Hewa-Kasakarage, N. N.; Zamkov, M. *J. Phys. Chem. C* **2008**, *112*, 9301–9307.
(96) Ivanov, S. A.; Piryatinski, A.; Nanda, J.; Tretiak, S.; Zavadil, K. R.; Wallace, W. O.; Werder, D.; Klimov, V. I. *J. Am. Chem. Soc.* **2007**, *129*, 11708–11719.
(97) Kirsanova, M.; Nemchinov, A.; Hewa-Kasakarage, N. N.; Schmall, N.; Zamkov, M. *Chem. Mater.* **2009**, *21*, 4305–4309.
(98) Johnston, K. W.; Pattantyus-Abraham, A. G.; Clifford, J. P.; Myrskog, S. H.; Hoogland, S.; Shukla, H.; Klem, J. D.; Levina, L.; Sargent, E. H. *Appl. Phys. Lett.* **2008**, *92*, No. 122111.
(99) Szendrei, K.; Gomulya, W.; Yarema, M.; Heiss, W.; Loi, M. A. *Appl. Phys. Lett.* **2010**, *97*, No. 203501.
(100) Luther, J. M.; Gao, J.; Lloyd1; Octavi, M. T.; Semonin, E.; Beard, M. C.; Nozik, A. J. *Adv. Mater.* **2010**, *22*, 3704–3707.